



Article

# Process Map Definition for Laser Metal Deposition of VDM Alloy 780 on the 316L Substrate

Pascal Paulus <sup>1,\*</sup>, Yannick Ruppert <sup>2</sup>, Michael Vielhaber <sup>1</sup> and Juergen Griebisch <sup>2</sup>

<sup>1</sup> Institute of Engineering Design, Saarland University, Campus E2 9, 66123 Saarbruecken, Germany

<sup>2</sup> School of Engineering, University of Applied Sciences Saarland, Goebenstrasse 40, 66117 Saarbruecken, Germany

\* Correspondence: paulus@kt.uni-saarland.de

**Abstract:** VDM Alloy 780 is a novel Ni-based superalloy that allows for approximately 50 °C higher operating temperatures, compared to Inconel 718, without a significant decrease in mechanical properties. The age hardenable NiCoCr Alloy combines increased temperature strength with oxidation resistance, as well as improved microstructural stability due to  $\gamma'$ -precipitation. These advantages make it suitable for wear- and corrosion-resistant coatings that can be used in high temperature applications. However, VDM Alloy 780 has not yet been sufficiently investigated for laser metal deposition applications. A design of experiments with single tracks on 316L specimens was carried out to evaluate the influence of the process parameters on clad quality. Subsequently, the quality of the clads was evaluated by means of destructive and non-destructive testing methods, in order to verify the suitability of VDM Alloy 780 for laser metal deposition applications. The single-track experiments provide a basis for coating or additive manufacturing applications. For conveying the results, scatter plots with regression lines are presented, which illustrate the influence of specific energy density on the resulting porosity, dilution, powder efficiency, aspect ratio, width and height. Finally, the clad quality, in terms of porosity, is visualized by two process maps with different mass per unit lengths.

**Keywords:** laser metal deposition; VDM Alloy 780; superalloy; 316L; process map; single track



**Citation:** Paulus, P.; Ruppert, Y.; Vielhaber, M.; Griebisch, J. Process Map Definition for Laser Metal Deposition of VDM Alloy 780 on the 316L Substrate. *J. Manuf. Mater. Process.* **2023**, *7*, 86. <https://doi.org/10.3390/jmmp7030086>

Academic Editor: Antonio Riveiro

Received: 22 March 2023

Revised: 11 April 2023

Accepted: 21 April 2023

Published: 26 April 2023



**Copyright:** © 2023 by the authors. Licensee MDPI, Basel, Switzerland. This article is an open access article distributed under the terms and conditions of the Creative Commons Attribution (CC BY) license (<https://creativecommons.org/licenses/by/4.0/>).

## 1. Introduction

In order to meet today's environmental and climate challenges, both the production processes and the resulting products must have an increased sustainability aspect. Additive manufacturing processes, in this case laser metal deposition (LMD), can make a decisive contribution here, as it enables the production of near-net-shape geometries without significant material waste [1] or graded materials [2], as well as cladding operations [3]. The resulting parts can have advanced properties due to the build-up of parts from various materials.

LMD enables a wide range of applications due to a large product range of available powder materials, such as repair [4–6], additive manufacturing [7–9] and cladding [10–13]. Research in this field includes parameter optimizations [14,15], simulation [16–18], process monitoring and control [19–22] and material structure, as well as mechanical properties [23–25]. The process variants of laser cladding can be differentiated in terms of the material supplied. A differentiation is made between powder-based and wire-based laser metal deposition [26]. Powder-based LMD uses powder particles that are injected into the process by means of a carrier gas. Typical powder grain fractions are between 50 and 100  $\mu\text{m}$  [27]. The feeding systems of additive materials in powder-based LMD processes can be divided into coaxial-continuous, coaxial-discontinuous and lateral systems [28].

Ni-based superalloys can be used for numerous applications, such as the manufacturing of static and rotating components in aircraft turbines [28,29], repair of gas turbines [30],

as well as wear- and corrosion-resistant coatings [31–33]. Most research in the field of LMD features Inconel 718 [34–36] or Inconel 625 [36–39]. A novel material that has hardly been used in the LMD process so far is VDM Alloy 780. The age-hardenable NiCoCr superalloy features increased temperature and oxidation resistance, as well as improved microstructural stability due to  $\gamma'$ -precipitation [40,41].

The objective of this work is to create a process map for powder-based LMD of the VDM Alloy 780 on the 316L substrate, to provide a basis for advanced processing applications in cladding or additive manufacturing. Due to the high number of process parameters, a process map is helpful to enable user-friendly production by predicting the quality of the clads [42]. The result of the deposition process depends on various process parameters, such as laser power, feed rate, powder mass flow, nozzle and carrier gas flow, stand-off distance, preheating temperatures, cooling rates and material properties. However, the main process parameters, i.e., laser power, feed rate and powder mass flow, are crucial for a qualitative results [43]. The quality of the clad is evaluated by the degree of dilution [44,45], density [46], cracks [47,48] and the microstructure. Furthermore, economical aspects such as powder efficiency and build rate are considered. In addition, economic aspects, such as powder efficiency and build-up rate, as well as the relationships between process parameters and quality characteristics, are taken into account. Finally, the results consist of multiple scatter plots and two process maps. The scatter plots are provided to show the relationships between quality criteria and specific energy density, while the process maps help in a defect-free deposition of VDM Alloy 780 on 316L.

## 2. Materials and Methods

### 2.1. Material Preparation

As additive, the gas-atomized age-hardenable VDM Alloy 780 (VDM Metals, Germany) with a grain size of 53–100  $\mu\text{m}$  is used. It is characterized by an austenitic microstructure, in which several phases can occur. The most important characteristic is the establishment of  $\gamma'$ -precipitation that replaces the  $\gamma''$ -hardening compared to known alloys, such as Inconel 718 [40]. While in Inconel 718 longtime exposure to temperatures above 650  $^{\circ}\text{C}$  leads to the transformation of the metastable  $\gamma''$ -phase and the loss of strengthening effects, VDM Alloy 780 features a higher temperature stability with excellent mechanical properties due to thermodynamically stable  $\gamma'$ -precipitation. The key difference of VDM Alloy 780 is the addition of Co, substituting Fe and Ni. This constrains the solvus temperature of the  $\gamma'$ -phase and consequently decelerates the precipitation [40]. The hardenability results from the alloy elements niobium, titanium and aluminum. Tillack [49] shows that increasing the contents of aluminum and titanium decreases the weldability, but increases the amount of strengthening  $\gamma'$ -precipitation. Studies on other age-hardenable Ni-based alloys with  $\gamma'$ -precipitation, such as Waspaloy [50] and IN 100 [51], have already been carried out. The chemical composition of the VDM Alloy 780 is listed in Table 1.

**Table 1.** Chemical composition (wt%) of the VDM Alloy 780.

Ni	Cr	Fe	C	Mn	Si	Cu	Mo	Co	Nb + Ta	Al	Ti	B	P	S
bal.	18	$\leq 4$	$\leq 0.1$	$\leq 0.5$	$\leq 0.3$	$\leq 0.5$	3	24	4–6	2	0.6	$\leq 0.02$	$\leq 0.03$	$\leq 0.015$

Figure 1 shows a comparison of the currently most used nickel-based superalloys in LMD. The dashed line indicates when an alloy is considered difficult to weld. As the figure shows, weldability is strongly influenced by the alloying elements aluminum and titanium. Due to its composition of 0.6 wt% Ti and 2 wt% Al, the VDM Alloy 780 exhibits significantly poorer weldability compared to Inconel 718 (IN 718). However, compared to U-700 and IN 100 alloys, it is still in a better weldability range.

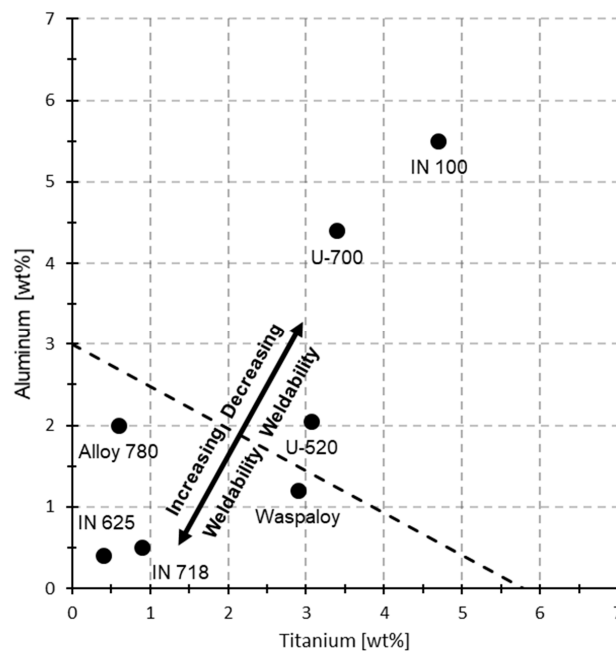


Figure 1. Weldability comparison of the most commonly used Ni-based superalloys in LMD [49].

As substrate material, an austenitic stainless steel (316L) with a thickness of 10 mm and a milled surface ( $R_a = 0.8 \mu\text{m}$ ) is used. Due to the excellent corrosion resistance and well-defined mechanical properties, these steels have a wide range of applications. For experimental preparation, the surface of the specimens was cleaned and degreased with ethanol. The chemical composition of 316L is listed in Table 2. The 316L was chosen as a substrate material because of its face-centered cubic lattice structure, as well as the comparable amount of Cr with regards to the VDM Alloy 780.

Table 2. Chemical composition (wt%) of the 316L substrate.

Ni	Cr	Fe	C	Mn	Si	Mo	P	S
12.5	17.5	bal.	0.03	2	1	2.5	0.045	0.03

### 2.2. Experimental Setup

The experimental setup features a Trumpf TruDisk 4001 solid-state laser as a beam source, with a maximum output power of 4000 W and a wavelength of  $\lambda = 1030 \text{ nm}$ . A 600  $\mu\text{m}$  fiber optic cable is used to guide this radiation to the optics. For the optics and nozzle, a Trumpf BEO D70 processing optic and an ILT SO 16 three-jet nozzle are used. The imaging ratio of 2:1 and an adjustable collimation allow for focusing the diameters of the laser beam between 1.2 and 8 mm. The SO 16 powder nozzle has a processing distance of 16 mm and a powder focus diameter of 4 mm. Thus, single-track widths of 1.5–7 mm were generated. The transport of the gas and powder to the process is ensured by the GTV PF 2/2 powder conveyor. The conveyor features two powder containers with different conveying volumes. The maximum conveying volume of the main container is 80 g/min. Both containers are operated with up to 12 l/min helium 4.6 as the carrier gas. Argon 4.6 with a flow rate of up to 20 l/min is used as a shielding gas. A KUKA KR 16-2 is used as the handling system for the laser cladding process.

### 2.3. Experimental Procedure

- The parameters for the experimental study are defined on the basis of the literature data for comparable materials such as Inconel 718 [29] and 625 [39]. In advance, the laser power is determined by an approximation equation based on literature informa-

tion [46]. The equation describes the required laser power as a function of machine- and material-specific factors. Radiation losses due to component reflection are not taken into account, since the assumption is made that these are nearly completely absorbed by the powder stream. For an economically optimized application, the following quality requirements are placed on the weld:

- To ensure that the powder is used optimally, the laser beam is adapted to match the constant powder focus diameter (4 mm), ensuring a nearly complete deposition of the additive.
- As quality characteristics, an aspect ratio of 4:1 [52] and a low degree of dilution (5–30%) [53] are desired.
- At the same time, high build-up rates should be realized in order to achieve an economical process.

Based on the limits of the experimental setup and the material properties of the VDM Alloy 780 and 316L, a laser power of approximately 3670 W at a track width of approximately 4 mm is required. As laser cladding is a multi-parameter problem and a new material pairing is used, a statistical experimental plan helps to efficiently implement the experiments. A design of experiments, based on the approximated initial parameters, is developed to investigate the influence of different energy densities at two constant mass per unit lengths (27.9 g/m and 39.3 g/m). The first mass per unit length was based on previously performed tests with Inconel 718 and process parameters selected from literature data [29]. The second mass per unit length was selected due to the poorer weldability of the VDM Alloy 780 compared to Inconel 718.

Based on the conclusion of Tillack [49] that the lower feed rates favor a more stable process, lower feed rates were investigated in the second part of the design of experiments. To ensure the comparability of the results, the specific energy density is retained. This results in a higher mass per unit length and a longer interaction time between the laser and the material.

The process parameters for laser power, feed rate and powder mass flow rate are shown in Table 3. Carrier, as well as shielding gas flow rates are kept constant. The carrier gas flow rate used is 4 l/min, while the shielding gas flow rate is 16 l/min. Additionally, to eliminate external interferences and process errors induced by the system, a block formation with randomization is carried out.

**Table 3.** Design of experiments to investigate the influence of different specific energy densities at a constant mass per unit length: (a) feed rates for 27.9 g/m; (b) feed rates for 39.3 g/m.

Laser Power [W]	Feed Rate [mm/min]		Powder Mass Flow Rate [g/min]	Specific Energy Density [kJ/g]
	(a)	(b)		
3000	1183	840	33	5.45
3250	1183	840	33	5.91
3500	1183	840	33	6.36
3750	1183	840	33	6.82
4000	1183	840	33	7.27
3000	1075	762	30	6.00
3250	1075	762	30	6.50
3500	1075	762	30	7.00
3750	1075	762	30	7.50
4000	1075	762	30	8.00
3000	968	690	27	6.67
3250	968	690	27	7.22
3500	968	690	27	7.78
3750	968	690	27	8.33
4000	968	690	27	8.89
3000	860	612	24	7.50
3250	860	612	24	8.13
3500	860	612	24	8.75
3750	860	612	24	9.38
4000	860	612	24	10.00

#### 2.4. Metallographic Preparation and Evaluation of Quality Characteristics

All specimens were cut on a cut-off machine, using a cut-off wheel with 250 mm outer diameter. Subsequently, the samples were warm-bedded. The metallographic preparation involved a series of three grinding steps (220, 500 and 1000) for five minutes each. After each grinding process, the specimens are cleaned in an ultrasonic bath with ethanol for five minutes. The specimens are then polished with a 3  $\mu\text{m}$  diamond polish for ten minutes. The polishing wheel is cleaned under water using detergent and a brush after each operation. The etching of the specimens was then carried out with V2A etchant for 45 s at 60 °C, which allows for both microstructural analysis and the investigation of flaws such as pores, bonding defects and cracks. The analysis of the cross-sections was carried out on a light microscope (Leica DM LM). In addition, the microstructure was examined with a scanning electron microscope (SEM) (JEOL 6460L), and energy-dispersive X-ray spectroscopy (EDX) analyses were performed. The quality characteristics considered are porosity, the degree of dilution, aspect ratio, powder efficiency, as well as the height and width of the seam.

The porosity  $\varepsilon_P$  provides information on how large the volume of the cavities is compared to the total volume of the clad. Pores and shrinkage cavities are formed during rapid solidification processes in which no outgassing of the molten material takes place and negatively affects the mechanical properties of the clad. The porosity of a welded clad can be calculated using the following Equation (1).  $A_P$  indicates the area of a pore in the cross section and  $A_T$  the total area of the clad [29].

$$\varepsilon_P = \frac{\sum A_P}{A_T} \quad (1)$$

In addition to porosity, the degree of dilution is an important parameter for assessing the quality of a clad. The degree of dilution indicates the percentage of the additive that does not directly build up the volume, but creates the bond between the substrate and the additive. The degree of dilution,  $A_D$ , of a clad can be calculated according to the following Equation (2).  $A_2$  indicates the cross-sectional area which does not cause a direct volume build-up and has immersed into the substrate material.  $A_1$  describes the cross-sectional area that is located above the substrate surface and achieves a volume build-up [54].

$$A_D = \frac{A_2}{A_1 + A_2} * 100\% \quad (2)$$

The aspect ratio,  $AR$ , provides information on the ratio of the width,  $W$ , to the height,  $H$ , of the clad and is calculated according to Equation (3). The ratio affects the tool path generation in coating and additive manufacturing applications, as the required overlap and layer height are affected.

$$AR = \frac{W}{H} \quad (3)$$

The powder efficiency indicates the percentage of the powder conveyed during the process that was effectively applied. The powder efficiency was calculated as the quotient of the applied mass  $m_A$  and the maximum applicable mass,  $m_{A,max}$ , according to Equation (4). The maximum applicable mass,  $m_{A,max}$ , can also be expressed as the product of the clad length,  $l$ , and powder mass flow rate,  $\dot{m}$ , divided by the feed rate,  $v$ .

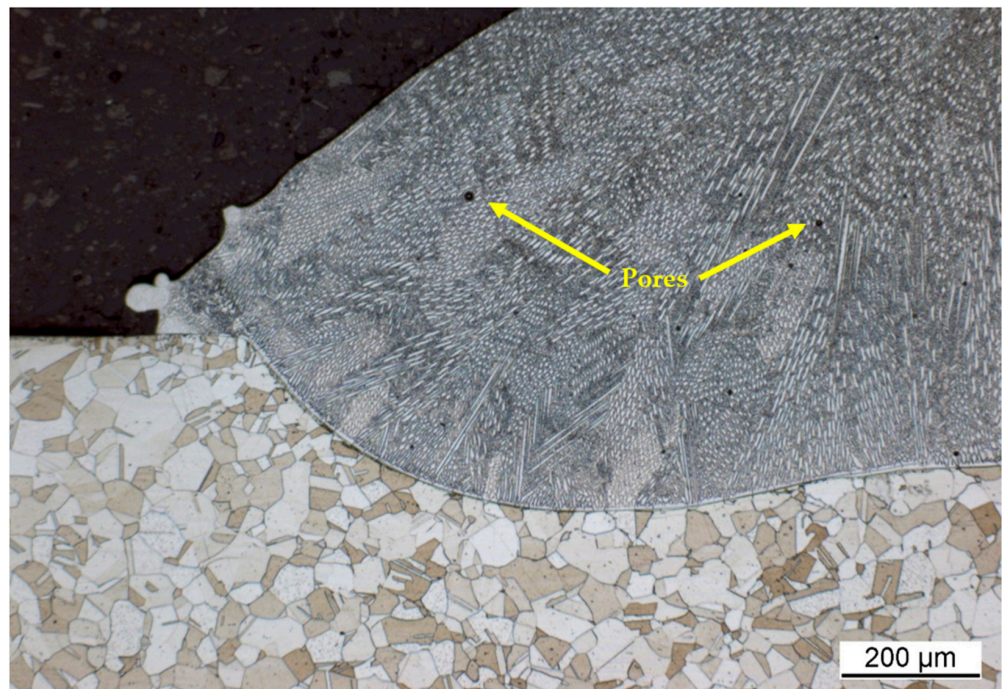
$$\eta_P = \frac{m_A}{m_{A,max}} = \frac{m_A * v}{l * \dot{m}} \quad (4)$$

### 3. Results and Discussion

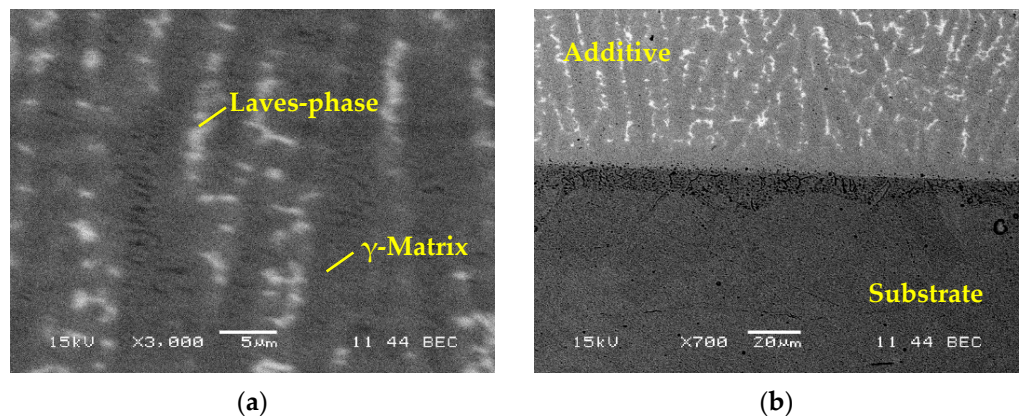
#### 3.1. Metallographic Analysis

Figure 2 shows a cross section of a specimen with the lowest porosity of 0.091%, an aspect ratio of 3.8, 30% dilution, 1.38 mm height and 5.25 mm width. The specimen was fabricated using a laser power of 3500 W, a feed rate of 612 mm/min and a powder mass

flow rate of 24 g/min. Spherical pores, but no cracks or bonding defects, were observed. The largest pore measured 17.2  $\mu\text{m}$  in diameter and no local concentration of pores could be detected in the entire cross section. The etching with V2A etchant for 45 s at 60  $^{\circ}\text{C}$  reveals a columnar grain structure characterized by elongated, epitaxial grain growth. A solidification structure with elongated grains growing in a normal direction to the substrate material was observed across all specimens. Additional bright interdendritic phases can be detected. These were further investigated by SEM analyses. Figure 3 presents the SEM micrographs of the microstructure of an as-deposited VDM Alloy 780 clad. Light gray precipitations that were analyzed using EDX show high amounts of Nb (approx. 22%). This phase is similar to the Laves phase and usually precipitates in alloys containing high amounts of Fe. EDX analyses of the dark-colored regions ( $\gamma$ -Matrix) show high amounts of Fe (approx. 10 to 15%) due to the intermixing of the substrate and the additive.



**Figure 2.** VDM Alloy 780 clad with a porosity of 0.091%, aspect ratio of 3.8, 30% dilution, 1.38 mm height and 5.25 mm width, etched with a V2A etchant (45 s at 60  $^{\circ}\text{C}$ ).



**Figure 3.** SEM image of a VDM Alloy 780 microstructure as built: (a) light gray precipitations are Nb-rich; (b) transition zone between the substrate and the applied material, no cracks can be detected.

### 3.2. EDX Linescan Analysis

Similar to Inconel 718, VDM Alloy 780 is a Nb-bearing, nickel-based superalloy. During LMD, the non-equilibrium solidification of the local molten pool leads to microsegregations of a high concentration of refractory elements such as Nb and eutectic Laves phases [55].

If different materials are used as substrates and additives, the mixing of the materials occurs in the dilution zone. Therefore, it is necessary to ensure that the mixing of the elements does not have a negative influence on the mechanical or chemical properties of the materials. A higher Fe content in Ni-based alloys, for example, promotes the formation of a Laves phase [56]. These brittle phases are crack-propagating, especially if they are precipitated in a chain-like manner [55].

Figure 4 shows that in the dilution zone, the amount of Fe changes. It can be observed that due to the LMD process, an increase in Fe within the additive has taken place. With a higher specific energy density, higher Fe contents can be detected in the additive. This value also strongly correlates with the dilution (Figure 5b). In order to achieve a low degree of dilution, lower specific energy densities are needed. This enables less mixing of the alloying elements, but results in higher porosity (Figure 5a). For the parameter sets applied, an increased amount of iron in the additive was detected in each specimen. The lowest Fe content (7.1%) was determined for a specific energy density of 5.45 kJ/g. The highest Fe content was observed at a specific energy density of 10 kJ/g, at 22.3%. EDX-based area determinations are averages, and local values may be higher. The Fe content in the LMD clad initially decreases steeply with the distance from the substrate, until a constant value is reached.

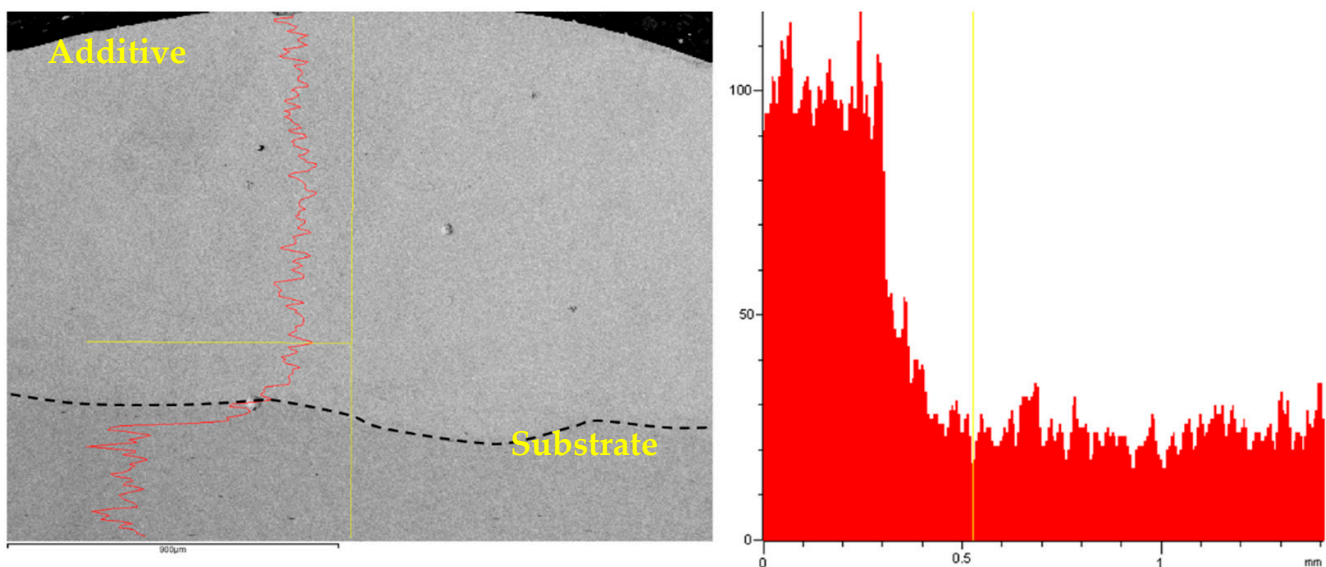


**Figure 4.** EDX linescan analysis of specimens with 6.67 kJ/g and 27.9 g/m, quantitative distribution of the iron content along the cross-section.

### 3.3. Statistical Analysis

The microscopic analyses of the clads show that there were no bonding defects, as well as cracking in the specimens. Figure 5 shows scatterplots of the results for the quality characteristics **porosity (a)**, **dilution (b)**, **powder efficiency (c)**, **aspect ratio (d)**, **width (e)** and **height (f)**. While **a–e** are mainly influenced by specific energy densities, **f** seems to be mainly influenced by the used mass per unit length. The regression analyses for **c** to **f**, on the other hand, show a linear relationship. A higher specific energy density results in a lower **porosity (a)** for both mass per unit lengths, which asymptotically approaches a value of 0.1% in this experimental study.

The **degree of dilution (b)** increases with a higher specific energy density, but converges to 38.2% for 27.9 g/m and 37% for 39.3 g/m for >10 kJ/g. In coating applications,

low mixing is desirable to avoid different chemical properties. In contrast, a higher degree of dilution has a positive effect on the bonding quality in additive manufacturing applications. High intermixing of the substrate and the additive leads to unstandardized alloys, in which phases and precipitates can form, which have a negative influence on, for example, the strength and corrosion resistance.

The **powder efficiency (c)**, as a function of specific energy density, indicates the largest deviation in the regression analysis (Pearson correlation  $r = 0.763$  for 27.9 g/m and  $r = 0.627$  for 39.3 g/m). Due to the low material deposition in relation to the substrate weight, the deposited mass can only be determined inaccurately. Nevertheless, it is observed that as the specific energy density increases, the powder efficiency also increases. In **a**, **b** and **c**, the mass per unit length is significantly responsible for the steepness of the regression line.

The **aspect ratio (d)** is an important characteristic for coating applications and additive manufacturing [45]. In pure coating applications, it has a decisive influence on the path calculation of the surface to be coated (overlap ratio). In the production of volumes, important path planning parameters are based on the aspect ratio in order to create near-net-shape geometries and be able to design the post-processing efficiently. The aspect ratio can be predicted for both mass flows via the regression equation, with an  $r = 0.913$  for 27.9 g/m and  $r = 0.893$  for 39.3 g/m.

With a mass per unit length of 39.3 g/m, an ideal ratio of 4:1 is achieved with a specific energy density of 8.5–10 kJ/g. In addition, a low porosity and high powder efficiency can be observed.

If the **width (e)** and **height (f)** are considered as separate characteristics, the resulting characteristic can be predicted more accurately for lower mass per unit lengths. The regression lines in **d**, **e** and **f** are parallel to one another. Here, the mass per unit length mainly influences the Y-axis intercept, and defines the start and end values for the selected mass flows. Based on the regression analyses and the requirements for a high quality clad, a target optimization can be defined, which suggests the processing of the VDM Alloy 780 with  $\geq 8.5$  kJ/g. At the same time, a larger mass flow results in higher build-up rates.

However, the maximum processing parameters, such as laser power, feed rate and powder mass flow, are system-dependent and must therefore be adapted to the existing system with reference to the available specific energy density.

The determined parameters of the single-track tests are only suitable to a limited extent for adaptation in the generative build-up of thin-walled structures or volumes. The temperature gradient generated during the additive manufacturing process has a detrimental effect on the microstructure and the residual stresses. Furthermore, shape deviations, as a result of local heat accumulation, are possible. However, the single-track experiments provide geometrical and metallurgical properties of the clad, which save time and materials for further investigations.

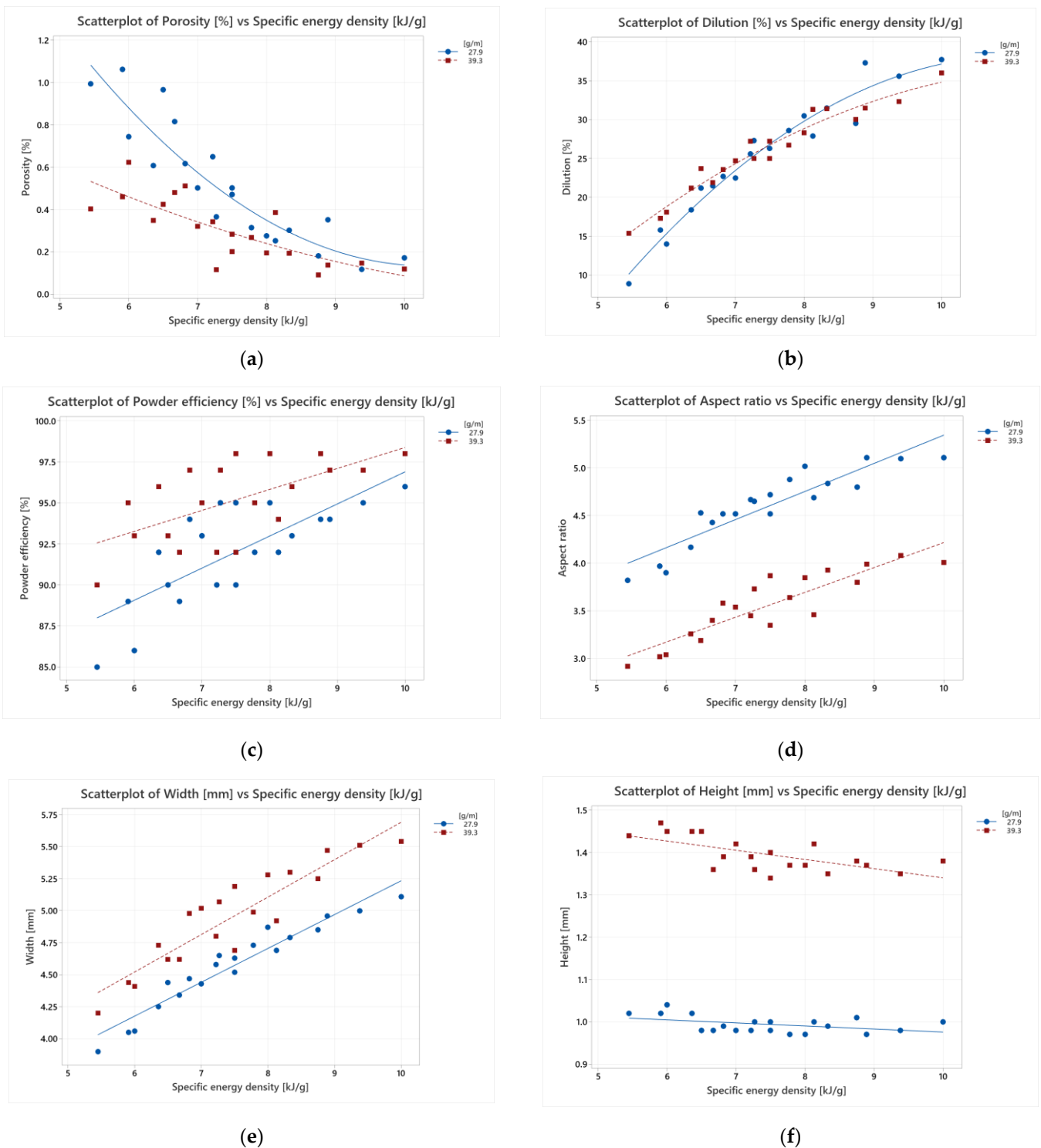


**Figure 5.** Scatterplots of quality characteristics vs. specific energy densities with 27.9 g/m (blue) and 39.3 g/m (red): (a) Porosity; (b) dilution; (c) powder efficiency; (d) aspect ratio; (e) width; (f) height.

### 3.4. Process Map Definiton

Figures 6 and 7 show two process maps for laser metal deposition of the VDM Alloy 780 using different mass per unit lengths. The investigations show that higher specific energy densities in combination with lower feed rates result in a lower porosity. Efficient deposition is possible with a higher mass per unit length, since lower porosity values can be achieved at the same build rate using a lower feed rate. The process window in Figure 7

already starts to open at a mass per unit length of 39.3 g/m from a level of 3400 W, allowing porosity values of less than 0.3% to be achieved. With a mass per unit length of 27.9 g/m, on the other hand, only a process window can be glimpsed in the upper left corner of Figure 6. Presumably, this window will open further by increasing the energy density; in other words, by increasing the laser power higher than  $P = 4000$  W or reducing the feed rate. Contrary to this, a reduction of the feed rate is also undesirable, since this would result in economic losses. Considering the build rate of the process additionally, an increase in the mass per unit length seems reasonable, since this keeps the build rate constantly high and a further reduction of the porosity can presumably take place at lower energy densities.

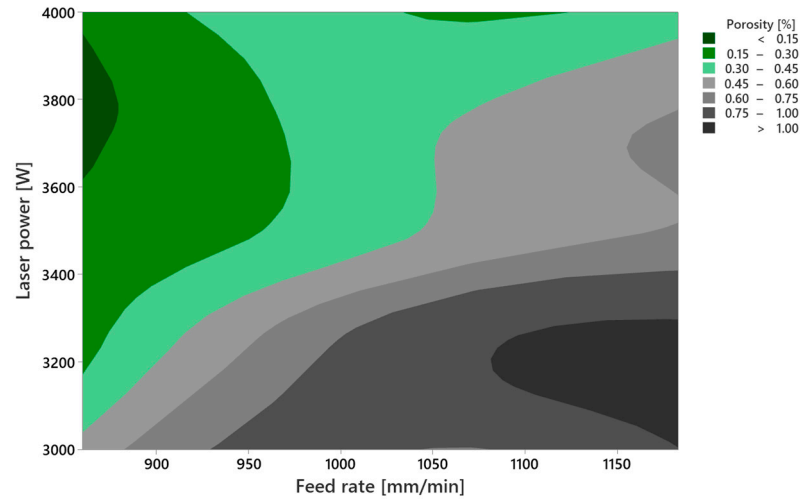


**Figure 6.** Process map of the VDM Alloy 780 regarding the feed rate and laser power, using a mass per unit length of 27.9 g/m.

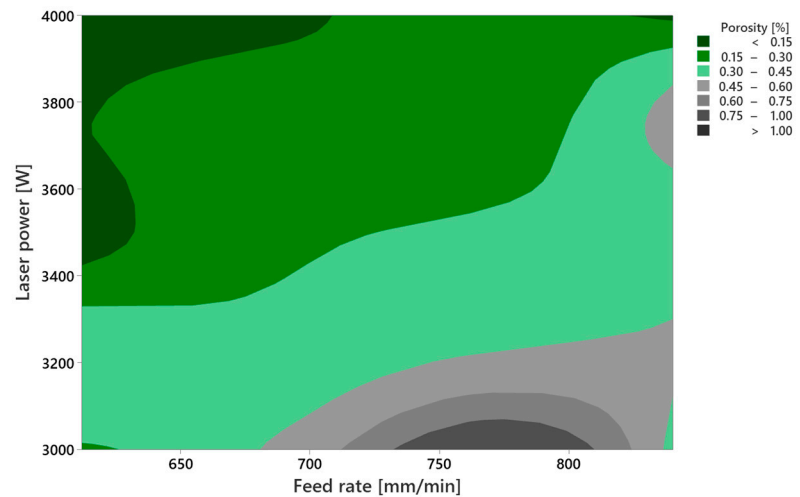


**Figure 7.** Process map of the VDM Alloy 780 regarding the feed rate and laser power, using a mass per unit length of 39.3 g/m.

#### 4. Conclusions

The aim of this work was to create a process map for single-track clads of the VDM Alloy 780 on the 316L substrate. The main process parameters, such as laser power, feed rate and powder mass flow rate, are used in the design of the experiments to investigate the influence of different specific energy densities at constant mass per unit lengths. The results of the investigation show that a high-quality clad with  $<0.15\%$  porosity can be achieved with 27.9, as well as 39.3 g/m. While the process window for economically efficient quality cladding is rather small at 27.9 g/m, higher mass per unit lengths seem to be advantageous

for processing with lower specific energy densities. Optimization with masses per unit length  $> 39.3$  g/m will further improve the economic efficiency of the process, as higher build rates can be realized. The most significant conclusions from the present study are as follows:

- In powder-based laser metal deposition of the VDM Alloy 780 on the 316L substrate, higher masses per unit length improve the overall porosity values.
- Higher mass per unit lengths are beneficial, since the degree of dilution is reduced at high specific energy densities with low porosity values [57]. In addition, the intermixing of the substrate and the additive must be kept low to avoid different chemical properties of the VDM Alloy 780 clads.
- A mass per unit length of 39.3 g/m with 8.75 kJ/g achieves high clad quality (0.091% porosity, aspect ratio of 3.8 and 30% dilution).
- The appearance of the Laves phase in deposited clads occurs due to the intermixing of the substrate and the additive.
- EDX analyses show that the Fe content strongly depends on the specific energy density of the process. The lowest Fe content of 7.1% was determined for a specific energy density of 5.45 kJ/g. The highest Fe content was observed at a specific energy density of 10 kJ/g, at 22.3%.
- In order to further reduce the porosity ( $<0.1\%$ ) and the Fe content in the clad, higher mass per unit lengths with lower feed rates should also be considered.

**Author Contributions:** P.P.: Conceptualization, Investigation, Methodology, Project administration, Formal analysis, Writing—original draft; Y.R.: Conceptualization, Investigation, Methodology, Visualization, Formal analysis, Writing—original draft; M.V.: Supervision, Resources, Writing—review and editing; J.G.: Supervision, Resources, Validation, Writing—review and editing. All authors have read and agreed to the published version of the manuscript.

**Funding:** This research was funded by European Regional Development Fund (ERDF), within the project “LPA2PECM”.

**Data Availability Statement:** The data presented in this study are available on request from the corresponding author.

**Conflicts of Interest:** The authors declare no conflict of interest.

## References

1. Heilemann, M.; Möller, M.; Emmelmann, C.; Burkhardt, I.; Riekehr, S.; Ventzke, V.; Kashaev, N.; Enz, J. Laser Metal Deposition of Ti-6Al-4V Structures: New building strategy for a decreased shape deviation and its influence on the microstructure and mechanical properties. In Proceedings of the Lasers in Manufacturing Conference, München, Germany, 26–29 June 2017.
2. Yan, J.; Battiato, I.; Fadel, G.M. Planning the process parameters for the direct metal deposition of functionally graded parts based on mathematical models. *J. Manuf. Process.* **2018**, *31*, 56–71. [[CrossRef](#)]
3. Güpner, M.; Patschger, A.; Bliedtner, J. Influence of Process Parameters on the Process Efficiency in Laser Metal Deposition Welding. *Phys. Procedia* **2016**, *83*, 657–666. [[CrossRef](#)]
4. Graf, B.; Gumenyuk, A.; Rethmeier, M. Laser Metal Deposition as Repair Technology for Stainless Steel and Titanium Alloys. *Phys. Procedia* **2012**, *39*, 376–381. [[CrossRef](#)]
5. Qi, H.; Azer, M.; Singh, P. Adaptive toolpath deposition method for laser net shape manufacturing and repair of turbine compressor airfoils. *Int. J. Adv. Manuf. Technol.* **2010**, *48*, 121–131. [[CrossRef](#)]
6. Graf, B.; Ammer, S.; Gumenyuk, A.; Rethmeier, M. Design of Experiments for Laser Metal Deposition in Maintenance, Repair and Overhaul Applications. *Procedia CIRP* **2013**, *11*, 245–248. [[CrossRef](#)]
7. Fu, Y.; Guo, N.; Wang, G.; Yu, M.; Cheng, Q.; Zhang, D. Underwater additive manufacturing of Ti-6Al-4V alloy by laser metal deposition: Formability, gran growth and microstructure evolution. *Mater. Des.* **2021**, *197*, 109196. [[CrossRef](#)]
8. Langebeck, A.; Bohlen, A.; Rentsch, R.; Vollertsen, F. Mechanical Properties of High Strength Aluminum Alloy EN AW-7075 Additively Manufactured by Directed Energy Deposition. *Metals* **2020**, *10*, 579. [[CrossRef](#)]
9. Gradl, P.; Tinker, D.C.; Park, A.; Mireles, O.R.; Garcia, M.; Wilkerson, R.; Mckinney, C. Robust Metal Additive Manufacturing Process Selection and Development for Aerospace Components. *J. Mater. Eng. Perform.* **2022**, *31*, 6013–6044. [[CrossRef](#)]
10. Amado, J.M.; Montero, J.; Tobar, M.J.; Yáñez, A. Laser Cladding of Ni-WC Layers with Graded WC Content. *Phys. Procedia* **2014**, *56*, 269–275. [[CrossRef](#)]

11. Janicki, D.; Górka, J.; Kotarska, A. Laser cladding of Inconel 625-based composite coatings. *Weld. Technol. Rev.* **2018**, *90*, 9. [[CrossRef](#)]
12. Łukasz, N.; Marta, W. Finishing Surface After Regeneration with Laser Cladding. *Procedia Eng.* **2017**, *192*, 1012–1015. [[CrossRef](#)]
13. Li, T.; Zhang, L.; Bultel, G.G.P.; Schopphoven, T.; Gasser, A.; Schleifenbaum, J.H.; Poprawe, R. Extreme High-Speed Laser Material Deposition (EHLA) of AISI 4340 Steel. *Coatings* **2019**, *9*, 778. [[CrossRef](#)]
14. Mahamood, R.M.; Akinlabi, E.T. Processing Parameters Optimization for Material Deposition Efficiency in Laser Metal Deposited Titanium Alloy. *Lasers Manuf. Mater. Process.* **2016**, *3*, 9–21. [[CrossRef](#)]
15. Caiazzo, F.; Alfieri, V.; Argenio, P.; Sergi, V. Additive manufacturing by means of laser-aided directed metal deposition of 2024 aluminium powder: Investigation and optimization. *Adv. Mech. Eng.* **2017**, *9*, 1687814017714982. [[CrossRef](#)]
16. Biegler, M.; Graf, B.; Rethmeier, M. In-situ distortions in LMD additive manufacturing walls can be measured with digital image correlation and predicted using numerical simulations. *Addit. Manuf.* **2018**, *20*, 101–110. [[CrossRef](#)]
17. Tamanna, N.; Crouch, R.; Naher, S. Progress in numerical simulation of the laser cladding process. *Opt. Lasers Eng.* **2019**, *122*, 151–163. [[CrossRef](#)]
18. Zeng, Q.; Tian, Y.; Xu, Z.; Qin, Y. Simulation of thermal behaviours and powder flow for direct laser metal deposition process. *MATEC Web Conf.* **2018**, *190*, 2001. [[CrossRef](#)]
19. Arrizubieta, J.I.; Martínez, S.; Lamikiz, A.; Ukar, E.; Arntz, K.; Klocke, F. Instantaneous powder flux regulation system for Laser Metal Deposition. *J. Manuf. Process.* **2017**, *29*, 242–251. [[CrossRef](#)]
20. Vandone, A.; Baraldo, S.; Valente, A.; Mazzucato, F. Vision-based melt pool monitoring system setup for additive manufacturing. *Procedia CIRP* **2019**, *81*, 747–752. [[CrossRef](#)]
21. Bi, G.; Gasser, A.; Wissenbach, K.; Drenker, A.; Poprawe, R. Identification and qualification of temperature signal for monitoring and control in laser cladding. *Opt. Lasers Eng.* **2006**, *44*, 1348–1359. [[CrossRef](#)]
22. Marko, A.; Bähring, S.; Raute, J.; Biegler, M.; Rethmeier, M. Quality Prediction in Directed Energy Deposition Using Artificial Neural Networks Based on Process Signals. *Appl. Sci.* **2022**, *12*, 3955. [[CrossRef](#)]
23. Jiang, B.; Zhengloung, L.; Xi, C.; Peng, L.; Nannan, L.; Yanbin, C. Microstructure and mechanical properties of TiB<sub>2</sub>-reinforced 7075 aluminum matrix composites fabricated by laser melting deposition. *Ceram. Int.* **2019**, *45*, 5680–5692. [[CrossRef](#)]
24. Li, L.; Wang, J.; Lin, P.; Liu, H. Microstructure and mechanical properties of functionally graded TiCp/Ti6Al4V composite fabricated by laser melting deposition. *Ceram. Int.* **2017**, *43*, 16638–16651. [[CrossRef](#)]
25. Loginova, I.S.; Khalil, A.M.; Churyumov, A.; Solonin, A.N.; Popov, N.A. Effect of Direct Laser Deposition on Microstructure and Mechanical Properties of 316L Stainless Steel. *KnE Eng.* **2019**, *1*, 82. [[CrossRef](#)]
26. Bambach, M.; Sizova, I.; Silze, F.; Schnick, M. Comparison of laser metal deposition of Inconel 718 from powder, hot and cold wire. *Procedia CIRP* **2018**, *74*, 206–209. [[CrossRef](#)]
27. Katayama, S. *Handbook of Laser Welding Technologies*; Woodhead Publishing: Cambridge UK; Philadelphia, PA, USA, 2013.
28. Kelbassa, I. Qualifizieren des Laserstrahl-Auftragsschweißens von BLISKS aus Nickel- und Titanbasislegierungen. Ph.D. Thesis, RWTH Aachen University, Aachen, Germany, 2006.
29. Witzel, J.M.F. Qualifizierung des Laserstrahl-Auftragsschweißens zur Generativen Fertigung von Luftfahrtkomponenten. Ph.D. Thesis, RWTH Aachen University, Aachen, Germany, 2014.
30. Petrat, T.; Graf, B.; Gumenyuk, A.; Rethmeier, M. Laser Metal Deposition as Repair Technology for a Gas Turbine Burner Made of Inconel 718. *Phys. Procedia* **2016**, *83*, 761–768. [[CrossRef](#)]
31. Rauter, R. Laserauftragsschweißen von Wolframkarbidschichten in Nickelbasismatrixen zur Herstellung Verschleißfester Beschichtungen von Warmformwerkzeugen. Master's Thesis, Technischen Universität Graz, Graz, Austria, 2016.
32. Amado, J.M.; Tobar, M.J.; Yáñez, A.; Amigó, V.; Candel, J.J. Crack Free Tungsten Carbide Reinforced Ni(Cr) Layers obtained by Laser Cladding. *Phys. Procedia* **2011**, *12*, 338–344. [[CrossRef](#)]
33. Luo, J.; Liu, X.-B.; Xiang, Z.-F.; Shi, S.-H.; Chen, Y.; Shi, G.-L.; Wu, S.-H.; Wu, Y.-N. Synthesis of High-Temperature Self-lubricating Wear Resistant Composite Coating on Ti6Al4V Alloy by Laser Deposition. *J. Mater. Eng. Perform.* **2015**, *24*, 1881–1889. [[CrossRef](#)]
34. Bold, M.-N.; Linnenbrink, S.; Pirch, N.; Gasser, A.; Mund, J.; Schleifenbaum, J.H. Powder based laser material deposition on edges. *J. Laser Appl.* **2020**, *32*, 32001. [[CrossRef](#)]
35. Liu, F.; Lyu, F.; Liu, F.; Lin, X.; Huang, C. Laves phase control of inconel 718 superalloy fabricated by laser direct energy deposition via  $\delta$  aging and solution treatment. *J. Mater. Res. Technol.* **2020**, *9*, 9753–9765. [[CrossRef](#)]
36. Ghiaasiaan, R.; Poudel, A.; Ahmad, N.; Gradl, P.R.; Shao, S.; Shamsaei, N. High Temperature Tensile and Fatigue Behaviors of Additively Manufactured IN625 and IN718. *Procedia Struct. Integr.* **2022**, *38*, 581–587. [[CrossRef](#)]
37. Artur, V.; Konstantin, B.; Anton, K.; Andrey, A.; Marina, G. Development of laser metal deposition process for a large IN625 part using small trial samples. *Procedia CIRP* **2020**, *94*, 310–313. [[CrossRef](#)]
38. Dutkiewicz, J.; Rogal, Ł.; Kalita, D.; Berent, K.; Antoszewski, B.; Danielewski, H.; Węglowski, M.S.; Łazińska, M.; Durejko, T.; Czujko, T. Microstructure and Properties of Inconel 625 Fabricated Using Two Types of Laser Metal Deposition Methods. *Materials* **2020**, *13*, 5050. [[CrossRef](#)]
39. Heilemann, M.; Prakash, V.J.; Beulting, L.; Emmelmann, C. Effect of heat accumulation on the single track formation during laser metal deposition and development of a framework for analyzing new process strategies. *J. Laser Appl.* **2021**, *33*, 12003. [[CrossRef](#)]
40. Rösler, J.; Hentrich, T.; Gehrman, B. On the Development Concept for a New 718-Type Superalloy with Improved Temperature Capability. *Metals* **2019**, *9*, 1130. [[CrossRef](#)]

41. Solís, C.; Munke, J.; Bergner, M.; Kriele, A.; Mühlbauer, M.J.; Cheptiakov, D.V.; Gehrman, B.; Rösler, J.; Gilles, R. In Situ Characterization at Elevated Temperatures of a New Ni-Based Superalloy VDM-780 Premium. *Met. Mater. Trans. A* **2018**, *49*, 4373–4381. [[CrossRef](#)]
42. Bax, B.; Rajput, R.; Kellet, R.; Reisacher, M. Systematic evaluation of process parameter maps for laser cladding and directed energy deposition. *Addit. Manuf.* **2018**, *21*, 487–494. [[CrossRef](#)]
43. Alvarez, P.; Montealegre, M.; Pulido-Jiménez, J.; Arrizubieta, J. Analysis of the Process Parameter Influence in Laser Cladding of 316L Stainless Steel. *J. Manuf. Mater. Process.* **2018**, *2*, 55. [[CrossRef](#)]
44. Song, B.; Hussain, T.; Voisey, K.T. Laser Cladding of Ni50Cr: A Parametric and Dilution Study. *Phys. Procedia* **2016**, *83*, 706–715. [[CrossRef](#)]
45. Xi, W.; Song, B.; Zhao, Y.; Yu, T.; Wang, J. Geometry and dilution rate analysis and prediction of laser cladding. *Int. J. Adv. Manuf. Technol.* **2019**, *103*, 4695–4702. [[CrossRef](#)]
46. Möller, M.L.B. *Prozessmanagement für das Laser-Pulver-Auftragschweißen*; Springer: Berlin/Heidelberg, Germany, 2021.
47. Alizadeh-Sh, M.; Marashi, S.; Ranjbarnodeh, E.; Shoja-Razavi, R.; Oliveira, J.P. Prediction of solidification cracking by an empirical-statistical analysis for laser cladding of Inconel 718 powder on a non-weldable substrate. *Opt. Laser Technol.* **2020**, *128*, 106244. [[CrossRef](#)]
48. Korsmik, R.; Klimova-Korsmik, O.; Valdaytseva, E.; Udin, I. Investigation of cracking causes during multi-pass laser cladding of heat-resistant single crystal nickel alloy. *Procedia CIRP* **2020**, *94*, 314–319. [[CrossRef](#)]
49. Tillack, D.J. Nickel alloys and stainless steels for elevated temperature service: Weldability considerations. In *Proceedings from Materials Solutions*; Nickel Development Institute: Toronto, ON, Canada, 1997.
50. Hussein, N.; Segal, J.; McCartney, D.G.; Pashby, I.R. Microstructure formation in Waspaloy multilayer builds following direct metal deposition with laser and wire. *Mater. Sci. Eng. A* **2008**, *497*, 260–269. [[CrossRef](#)]
51. Acharya, R.; Das, S. Additive Manufacturing of IN100 Superalloy Through Scanning Laser Epitaxy for Turbine Engine Hot-Section Component Repair: Process Development, Modeling, Microstructural Characterization, and Process Control. *Met. Mater. Trans. A* **2015**, *46*, 3864–3875. [[CrossRef](#)]
52. Jambor, T. Funktionalisierung von Bauteiloberflächen Durch Mikro-Laserauftragschweißen. Ph.D. Thesis, RWTH Aachen University, Aachen, Germany, 2012.
53. Hügel, H.; Graf, T. *Laser in der Fertigung: Strahlquellen, Systeme, Fertigungsverfahren*, 2nd ed.; neu bearb. Aufl; Vieweg + Teubner: Wiesbaden, Germany, 2009.
54. Guepner, M.; Rietzke, S.; Paetzold, R.; Bliedtner, J.; Bergman, J.P. Process characterization of powder based laser metal deposition on thin substrates. *J. Laser Appl.* **2018**, *30*, 32506. [[CrossRef](#)]
55. Liu, X.; Xiao, H.; Xiao, W.; Song, L. Microstructure and Crystallographic Texture of Laser Additive Manufactured Nickel-Based Superalloys with Different Scanning Strategies. *Crystals* **2021**, *11*, 591. [[CrossRef](#)]
56. Maier, H.J.; Niendorf, T.; Bürgel, R. *Handbuch Hochtemperatur-Werkstofftechnik: Grundlagen, Werkstoffbeanspruchungen, Hochtemperaturlegierungen und -Beschichtungen*, 6th ed.; überarbeitete und erweiterte Auflage; Springer Vieweg: Wiesbaden, Germany; Heidelberg, Germany, 2019.
57. Moussaoui, K.; Rubio, W.; Mousseigne, M.; Sultan, T.; Rezai, F. Effects of Selective Laser Melting additive manufacturing parameters of Inconel 718 on porosity, microstructure and mechanical properties. *Mater. Sci. Eng. A* **2018**, *735*, 182–190. [[CrossRef](#)]

**Disclaimer/Publisher’s Note:** The statements, opinions and data contained in all publications are solely those of the individual author(s) and contributor(s) and not of MDPI and/or the editor(s). MDPI and/or the editor(s) disclaim responsibility for any injury to people or property resulting from any ideas, methods, instructions or products referred to in the content.